

Data capacity scaling of a distributed Rydberg atomic receiver array

J. Susanne Otto,^{a)} Marisol K. Hunter, Niels Kjærgaard, and Amita B. Deb^{b)}

Department of Physics, QSO-Centre for Quantum Science, and Dodd-Walls Centre, University of Otago, Dunedin, New Zealand

(Dated: April 8, 2021)

The data transfer capacity of a communication channel is limited by the Shannon-Hartley theorem and scales as $\log_2(1 + \text{SNR})$ for a single channel with the power signal-to-noise ratio (SNR). We implement an array of atom-optical receivers in a single-input-multi-output (SIMO) configuration by using spatially distributed probe light beams. The data capacity of the distributed receiver configuration is observed to scale as $\log_2(1 + N \times \text{SNR})$ for an array consisting of N receivers. Our result is independent on the modulation frequency, and we show that such enhancement of the bandwidth cannot be obtained by a single receiver with a similar level of combined optical power. We investigate both theoretically and experimentally the origins of the single channel capacity limit for our implementation.

I. INTRODUCTION

In recent years there has been a growing interest in atom-based techniques for the detection of microwave (MW) electric fields^{1,2}, that allow for calibration free SI-traceable measurements³ achieving ultra-high sensitivity⁴. Rydberg atoms have been identified as particularly suitable for such measurements of radio-frequency (RF) electric fields due to their high polarizabilities and large microwave (MW) transition dipole moments⁵. Advances in Rydberg based field measurements have been accompanied by applications in atom-based communication technology. The fundamental working principles of analog and digital communication, where a baseband signal is modulated onto an electromagnetic MW carrier wave, have recently been demonstrated in a range of Rydberg-based systems. Examples include amplitude modulation (AM)^{6–10}, frequency modulation (FM)^{11,12} and phase detection^{13,14}, as well as multiple bands¹¹, multiple channels¹⁵, and multiple species¹⁰. Common to these methods is the broad carrier frequency range from tens of MHz to several THz that can be covered by the numerous Rydberg states of a single atomic species.

Rydberg receivers generally rely on the phenomenon of electromagnetically induced transparency (EIT)¹⁶ in a three-level system, where a coupling laser field renders an otherwise opaque atomic medium transparent to a probe laser field due to quantum interference. If the three-level atomic system is coupled to a fourth level via an RF transition, the Autler-Townes (AT) effect¹⁷ alters the transmission of a light field. For an RF electric field, which is modulated with a signal, measuring the modulation of the transmitted light allows to directly retrieve the signal. In contrast to conventional receivers which rely on

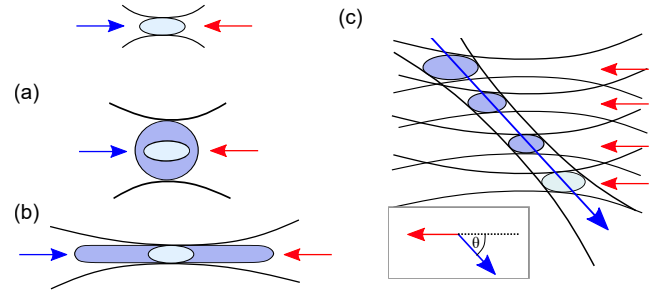


Figure 1. Possible scenarios for increasing the atomic volume of a Rydberg receiver (top). (a) Counter-propagating setup of probe (red) and coupling beam (blue) with larger beam diameters. (b) Counter-propagating beam setup with stretched optical path lengths of probe and coupling beam. (c) Setup with several parallel probe beams and a single coupling beam passing through the probe beams under an angle $\theta > 0$.

band-specific electronic components, Rydberg-based receivers benefit from a direct and real-time readout of information, and physical reconfiguration is not necessary when the carrier frequency is varied. Also, the received information is encoded in a light field, i.e., a laser beam, suitable for long-distance transport via a fiber-link.

One of the most important figures of merit for a communication system is the channel capacity, which gives the amount of information that can be passed through a communication channel in a period of time without error. For a channel with a bandwidth (BW) its upper limit is defined by the Shannon-Hartley theorem¹⁸ as

$$C = \text{BW} \times \log_2(1 + \text{SNR}) \quad (\text{bits/s}). \quad (1)$$

The crucial parameter for a communication system is therefore the power signal-to-noise ratio (SNR) at a given bandwidth, which has to be maximised in order to attain the maximal channel capacity. A common method for increasing the data transmission capability is to establish multiple channels using, e.g., multiple transmitter and

^{a)}susanne.otto@postgrad.otago.ac.nz

^{b)}amita.deb@otago.ac.nz

receiver antennas. A particularly successful technique for fulfilling demands of high data throughput rates and overall capacity are multi-input-multi-output (MIMO) systems¹⁹, and are widely used in telecommunication. MIMO devices employ arrays of receivers which are responsive to multiple simultaneous and independent data streams from multiple transmitter antennas, exploiting multipath propagation. A building block in the context of MIMO technology is a single-input-multi-output (SIMO) arrangement, where the receiver diversity is increased, but the transmitter kept to a single antenna. This arrangement is formally equivalent to a single receiver with an increased SNR, and therefore a higher data capacity is achieved. For N receiver antennas the data capacity increases with²⁰

$$C_A(N) = \text{BW} \times \log_2(1 + N \times \text{SNR}). \quad (2)$$

In this paper we investigate the scalability of the data capacity of atomic radio receivers in a regime where the receivers are independent of one another and are nearly identical. This, as mentioned above, realises a stepping stone towards MIMO system, where independent and spatially isolated receivers are a necessity.

As opposed to conventional antennas, Rydberg receivers can work in the electrically small regime²¹. Therefore it is possible, in principle, to improve the data capacity by increasing the atomic density within the receiver volume. In a vapour cell environment, this usually means that one needs to increase the vapour pressure within the cell by heating it which introduces significantly larger Doppler width and collisional broadening of the transition. Alternatively, the receiver volume can be expanded. This can, for example, be done by using larger beam diameters [see Fig. 1(a)], but comes with the drawback of requiring higher coupling laser powers to maintain high coupling laser powers. Another option is to extend the optical path length of probe and coupling beam, see Fig. 1(b). While this can initially increase the SNR, it also causes the background optical depth, which does not contribute to the signal, to rise, resulting in a drop of SNR. This can be counteracted by increasing the probe beam power to begin with, but the SNR will always reach a limit beyond a certain probe beam power for a given coupling laser power. The data capacity for the aforementioned configurations will vary greatly with the geometry of the setup, as the expanded atomic volumes spatially adjoin the original volume and are not necessarily independent of each other, and therefore do not constitute independent receivers.

Here we report on an experimental implementation of an array of independent Rydberg receivers that are nearly identical, and therefore accomplish a step towards a MIMO atomic receiver system. This is realised by introducing a small angle between the coupling and probe laser beams as schematically shown in Fig. 1(c) and without the demand for a higher coupling laser power. We show that this SIMO system follows the well-

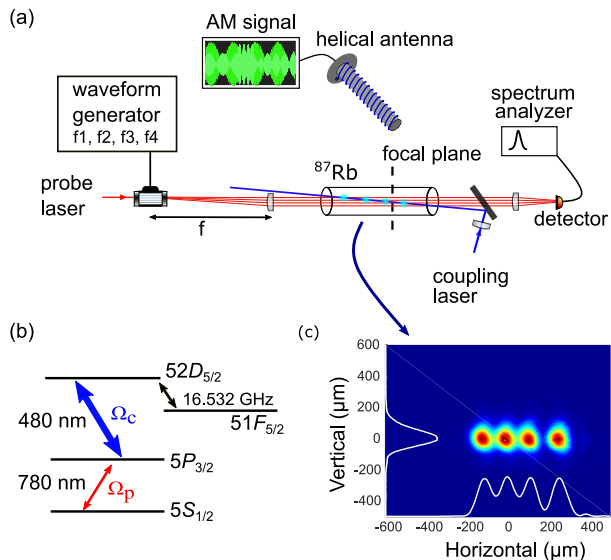


Figure 2. (a) Experimental setup used in this work and described in the text. (b) Four-level energy diagram for our atomic ^{87}Rb system. Ω_p and Ω_c denote the probe and coupling Rabi frequencies. (c) Beam profiles of four probe beams in the focal plane with frequency differences $f_1 - f_2 = f_2 - f_3 = 3 \text{ MHz}$ and $f_4 - f_3 = 4 \text{ MHz}$.

described data capacity scaling with the number of independent receiver volumes, confirming their independence. Specifically, we employ up to four distributed receiver volumes within a single vapour cell and we observe a $\log_2(1 + N \times \text{SNR})$ scaling of the data capacity, where N is the number of spatially distributed receivers.

II. EXPERIMENTAL SETUP

The heart of our experimental setup, see Fig. 2(a), is a 75 mm-long, 25 mm-diameter cylindrical vapour cell containing rubidium (Rb) atoms. The Rb atoms serve as receiver medium for an AM microwave signal emitted by a helical antenna. The AM microwave electric field is optically detected in a ladder-type Rydberg-EIT scheme, where a strong coupling field generates a transparency window on resonance in presence of a weak probe field, see Fig. 2(b). This allows to transduce AM information in the RF domain to optical information encoded as a change of the probe transmission.

In our setup the coupling laser has a wavelength of 480 nm and a power of 22 mW, and is focused to a waist of $60 \mu\text{m}$ in the vapour cell. This corresponds to a Rayleigh length of $\sim 25 \text{ mm}$ and a Rabi frequency of $2\pi \times 8 \text{ MHz}$ for the transition $5P_{3/2} \leftrightarrow 52D_{5/2}$. A probe light field at 780 nm passes through an acousto-optic modulator (AOM), which is driven by a multitone frequency source. Up to four diffracted beams at frequencies f_1, f_2, f_3 and f_4 can be generated simultaneously. The diffracted beams impinge on a lens which

generates parallel beams with $\sim 70 \mu\text{m}$ radii in its focal plane, see Fig. 2(c). The probe and coupling beams are counter-propagating under an angle of $\sim 2^\circ$ to create spatially separated ($> 3 \text{ mm}$) and independent overlap areas between the coupling and probe beams. The transmission signal of the probe beams is collected by a lens and focused onto a photodetector. For the purpose of retrieving the frequency and amplitude of the modulation signal the photodetector is connected to a spectrum analyser.

For the frequency stabilisation of the probe and coupling lasers, two auxiliary Rb vapour cells are employed. The probe laser is stabilized to a saturated absorption spectroscopy signal of the ^{87}Rb D₂-line. With the AOM in front of the experimental cell, see Fig. 2(a), we obtain four beams with frequencies close to the transition $5S_{1/2}(F=2) \rightarrow 5P_{3/2}(F'=3)$. For the stabilisation of the tuneable coupling laser the EIT signal of a μ -metal-shielded Rb vapour cell is used, and the laser can be stabilized to different Rydberg levels $nD_{5/2}$ and $nD_{3/2}$ with $n = 30$ to 70. For the results presented in this paper we use the Rydberg level $52D_{5/2}$.

Our experimental vapour cell is kept at a temperature of 85°C yielding a ground state atom density of $\sim 10^{12}\text{cm}^{-3}$ for a ^{87}Rb sample. The two optical fields which are passing through the cell are coupled to the Rydberg level $51F_{5/2}$ with a MW carrier field at 16.532 GHz . This field is generated by an analog signal generator that feeds a 10 dBm signal into a home-built helical end-fire antenna. In axial mode the antenna radiates microwave fields along the helical axis and the radiation is circularly polarized. The antenna is located 30 cm from the vapour cell. With increasing field strength of the MW field, the amplitude of the EIT signal decreases while its width broadens and for MW electric fields $> 10 \text{ dBm}$ our transmission signal splits into two AT peaks. The MW carrier field is amplitude modulated with a sinusoidal signal with frequencies between 100 kHz and 1 MHz . This results in a variation of the transmission of the probe fields, which can be directly measured with the combination of photodetector and spectrum analyser and permits to retrieve the initial AM signal.

III. RESULTS

A. SNR and Bandwidth of a Single Receiver

Figure 3(a) shows the demodulated probe signal for a carrier field amplitude modulated at 200 kHz , measured with the spectrum analyser for a resolution bandwidth of 3 kHz . The transmitted probe field is detected by the photodetector, and the spectrum analyser yields the power spectral density for frequencies between 100 and 350 kHz . The traces have distinct maxima at the modulation frequency, which are standing out against the noise floor observed with the spectrum analyser. We define the SNR_{dB} as the difference of the power spectral density at the modulation frequency to the noise floor on the spec-

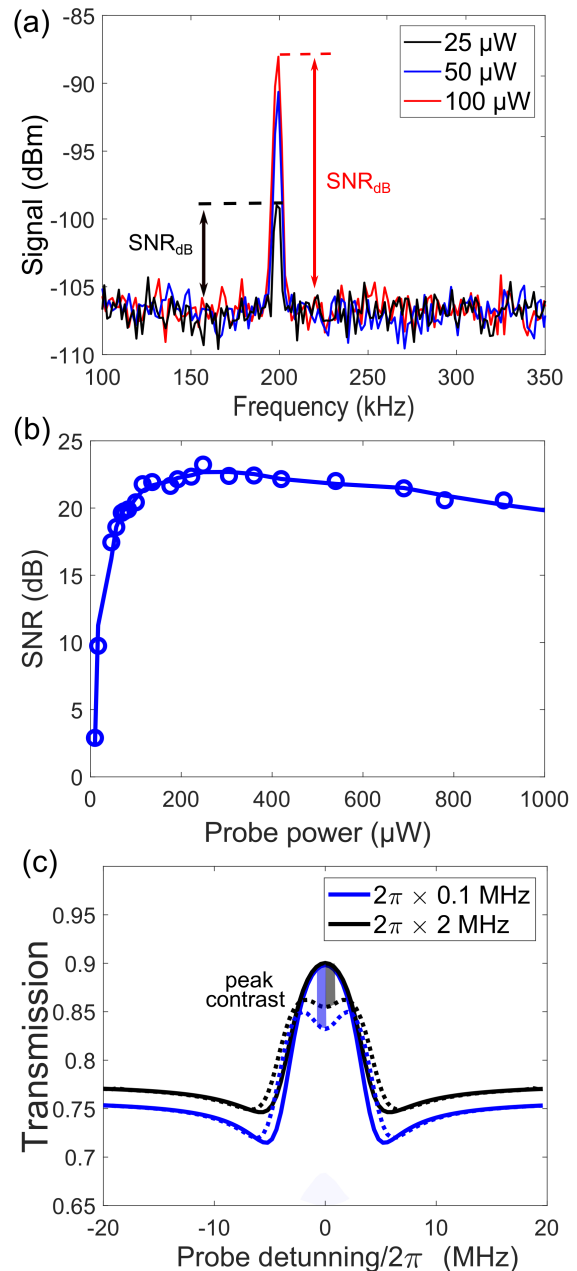


Figure 3. (a) Demodulated signal of the probe transmission as a function of frequency measured with the spectrum analyser for three different probe powers. (b) Dependence of the SNR_{dB} on the probe power for an AM frequency of 200 kHz . (c) Numerical data for the probe detuning versus probe transmission for two different probe Rabi frequencies (blue and black), in the EIT regime (solid lines) and AT regime (dotted lines) for a resonant RF field ($\Omega_{\text{RF}} = 2\pi \times 5 \text{ MHz}$).

trum analyser at the respective frequency in absence of the modulation. As can be seen from Fig. 3(a), the signal height and along with it the SNR_{dB} grow with increasing probe power in the presented scenario (black to red). The development in SNR_{dB} as a function of probe power is shown in more detail in Fig. 3(b). Initially, the SNR_{dB}

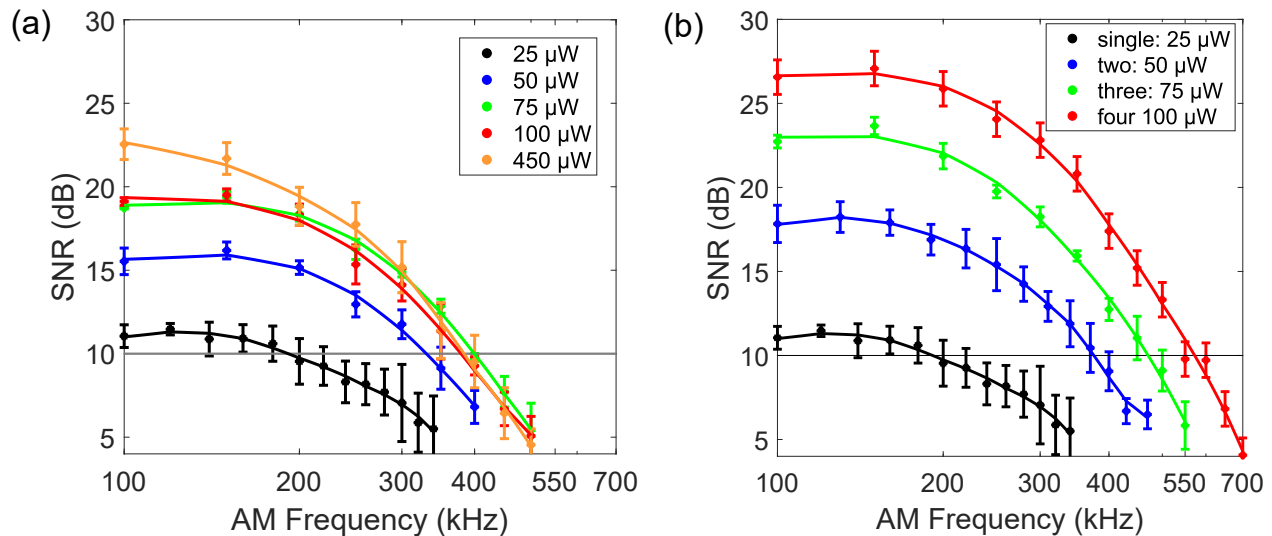


Figure 4. (a) SNR_{dB} as a function of AM frequency of the carrier MW field for different power levels of a single probe beam. The plot shows average values of four probe beams with frequency offsets to the resonance of -4.5 MHz, -1.5 MHz, 1.5 MHz and 5.5 MHz. (b) SNR_{dB} as a function of AM frequency for combinations of up to four probe beams of 25 μW with frequency offsets to the resonance frequency of $f_1 = -4.5$ MHz, $f_2 = -1.5$ MHz, $f_3 = 1.5$ MHz and $f_4 = 5.5$ MHz. Measurements were taken for all combinations of f_1, f_2, f_3, f_4 and average values and corresponding standard deviations are presented. The curves, obtained from a Savitzky–Golay filter, are to guide the eyes.

grows with increasing probe power, but reaches a maximum at ~ 150 μW , after which it slowly decreases for even higher probe powers, if the experimental conditions, i.e. atomic density and coupling power are kept identical. The growth of the SNR_{dB} with probe power is related to an increase in peak contrast, as illustrated in Fig. 3(c), which is the difference between the probe transmissions at the EIT peak in presence and absence of the carrier RF field. In the four level scheme in Fig. 2(b), the applied RF field suppresses the EIT transmission on resonance as shown as dotted lines in Fig. 3(c) for two different probe Rabi frequencies (black and blue). For strong RF fields the EIT transmission on resonance is suppressed and can reach the baseline, which is given by the absorption of the probe beam without RF and coupling field.

The development of peak contrast with probe power ($\propto \Omega_p^2$) can be qualitatively explained as follows: For larger Ω_p , power broadening leads to an increase of the spectral width of the atomic absorption line, resulting in an increased transmission of the probe beam and a rising baseline transmission. At the same time, for a fixed Rabi frequency of the coupling field, Ω_c , and weak Ω_p the population of the meta-stable Rydberg state increases with Ω_p , since the population ratio between the ground and Rydberg state is determined by Ω_p^2/Ω_c^2 . If less atoms are in the ground state the transmission of the probe field increases. Overall this results in a larger EIT peak²², and the observed initial rise of the SNR_{dB} in Fig. 3(b). As the number of atoms in the receiver volume is kept constant, the EIT peak transmission saturates²³ for even larger Ω_p while the two-level baseline transmission con-

tinues to grow, see Fig. 3(c). In our setup the noise floor on the spectrum analyser rises as a quadratic function of the probe power for > 50 μW , see Fig. 8 in the Appendix A, and limits the achievable SNR_{dB} for higher probe powers. The dominant mode of noise in our experiment is introduced by an AOM which is far above that posed by photon shot noise (more discussed in Appendix A). This explains the slow fall off of the SNR_{dB} for probe powers > 150 μW .

In addition to the probe power, the achievable SNR_{dB} depends on the modulation frequency of the carrier RF field, as shown in Figure 4(a). The fall-off of the SNR_{dB} with increasing AM frequency sets the bandwidth of the receiver system. We define the BW limit as the cutoff point with $\text{SNR}_{\text{dB}} = 10$ dB. Figure 4(a) shows a measurement of the BW for a single probe beam and five different probe powers. For faster modulations the SNR_{dB} decreases and reaches its BW limit at 380 kHz for probe powers ≥ 100 μW . The slope of the SNR-curves is determined by atomic parameters such as decoherence rates set by Doppler broadening and transit times, which are the same for all SNR-curves in Fig. 4(a). Increasing the SNR_{dB} initially improves the cut-off frequency, but as the SNR_{dB} reaches its maximum the BW saturates.

B. Multiple Atomic Receivers

With the objective to obtain independent detection volumes within our vapour cell, we distribute the power of our single probe beam over multiple probe beams. In

combination with a single coupling beam we obtain up to four simultaneous and nearly identical receiver volumes. We use AOM driving frequencies with $\Delta f = 3 - 4$ MHz between adjacent probe beams and observe a spatial separation of $\sim 100 \mu\text{m}$ in the focal plane, see Fig. 2(c). We establish a single-input-multi-output (SIMO) configuration, as it is used in the context of smart antenna technology for improved wireless communication performance. Figure 4(b) shows the SNR_{dB} versus AM frequency for one, two, three and four probe beams with individual powers of $25 \mu\text{W}$ at their probe frequencies f_1 to f_4 . The SNR_{dB} drops towards higher AM frequency, similar to the scenario for a single receiver in Fig. 4(a), since the slope of the SNR-curves is determined by the atomic parameters of our experimental setup. Crucially, however, the saturation of the EIT peak transmission for a single beam can be avoided. This allows us to exceed the BW limit of the single beam setup, as shown in Fig. 5. While for two beams the BW limit approximately matches the scenario of a single beam with twice the power, a clear improvement in BW appears for $N \geq 3$, where N is the number of beams. Overall, the maximum values of the SNR_{dB} and bandwidth for the single beam setup can be exceeded.

Assuming that two receiver areas are independent and have identical parameters such as Ω_p , Ω_c , beam frequencies, waists, and atomic densities, the signal amplitude increases by a factor of two. We note that doubling the optical power that contributes to the signal increases the SNR_{dB} by a factor of 4 (roughly 6 dB), as e.g. found in Fig. 4(a) (black to blue line). This is because the optical power P_{op} hitting the photodetector translates into a voltage $V \propto P_{\text{op}}$, and the spectrum analyser measures the corresponding electric power P_{el} , for which $P_{\text{el}} \propto V^2$. In Fig. 5(a) we show the increase in BW for up to four beams. As expected (see Appendix B) the BW scales logarithmically (black line), and exceeds the maximum bandwidth of the single receiver (blue shaded area).

The achievable data capacity for our system with N independent receiver volumes at a given amplitude modulation frequency f_{AM} transforms from Eq. (2) to

$$C_A(N) = f_{\text{AM}} \times \log_2(1 + N \times \text{SNR}_{N=1}). \quad (3)$$

Figure 5(b) presents the data capacity for three different modulation frequencies and up to four beams. The data capacity shows significant enhancement, following the predicted behaviour of Eq. (3) (dashed lines). Moreover the data capacity depends on the amplitude modulation frequency, as presented in Fig. 5(c). For low AM frequencies the data capacity has a linear dependence on the modulation frequency. For faster modulations the data capacity reaches a maximum, before decreasing due to the decreasing SNR_{dB} caused by a finite atom-switching time. The maximum of the data capacity moves towards higher modulation frequencies with the number of probe beams, N , as the SNR_{dB} increases with N .

The maximum values for bandwidth (~ 560 kHz) and data capacity (~ 1.3 Mbits/s) achieved in this setup are

rather low in comparison to other experiments⁷. This is predominantly caused by the angled geometry of the setup (see Fig. 1), and is discussed in more detail in Sec. III C 1. Importantly, for our current study bandwidth and channel capacity scale in a predictable manner with the number of receiver volumes, as the receiver volumes are independent.

C. Characterisation of the Distributed Receivers Setup

1. Effects of the angled configuration

The coupling laser power for our setup is limited to 22 mW. For the purpose of achieving independent receiver volumes without a need for several coupling laser beams, the coupling and probe laser beams are configured to counter-propagate under a small angle, so that one coupling beam is used for all receiver volumes. The angled geometry comes with the drawback of decreasing the SNR for the independent receiver volumes. This is a consequence of an additional Doppler shift²⁴, which broadens the linewidth of the EIT signal. In our setup, see Fig. 1(c), an angle of $\theta \approx 2^\circ$ results in a EIT linewidth that is approximately twice as large as for $\theta = 0^\circ$. However, while we do see a broadening of the EIT linewidth for $\theta > 0^\circ$, we do not see any additional change while using multiple probe beams. Therefore, we realise a setup with independent receivers as different groups of atoms are addressed within the vapour cell at the same instant of time. Another factor to consider is probe signal loss due to scattering of the probe light with atoms outside the sensing area. The length of the sensing area is with ~ 1 mm small in comparison to the full path length of the probe beams in the 75 mm long vapour cell.²⁵ This problem could be avoided in future realisations by using miniaturised vapour cells.

The scope of this paper is to investigate the scalability of the data capacity for a Rydberg-atom based SIMO system. Therefore the independence of the receiver volumes is of greater significance than high signal-to-noise ratios. With an average atomic velocity of ~ 150 m/s, adjacent receiver spacings exceeding 3 mm, and amplitude modulation frequencies of > 100 kHz, interactions due to atoms transiting between sensor areas are negligible. Because of the angled geometry the SNRs of the atomic volumes are overall low, but the configuration allows to establish the scaling law for the channel capacity of a SIMO setup.

2. Deviations of EIT peak heights for different receiver volumes

Unlike in an idealized scenario with identical distributed receivers, in our experimental setup the receiver volumes differ slightly due to the geometry of the setup and since the probe power is distributed via an

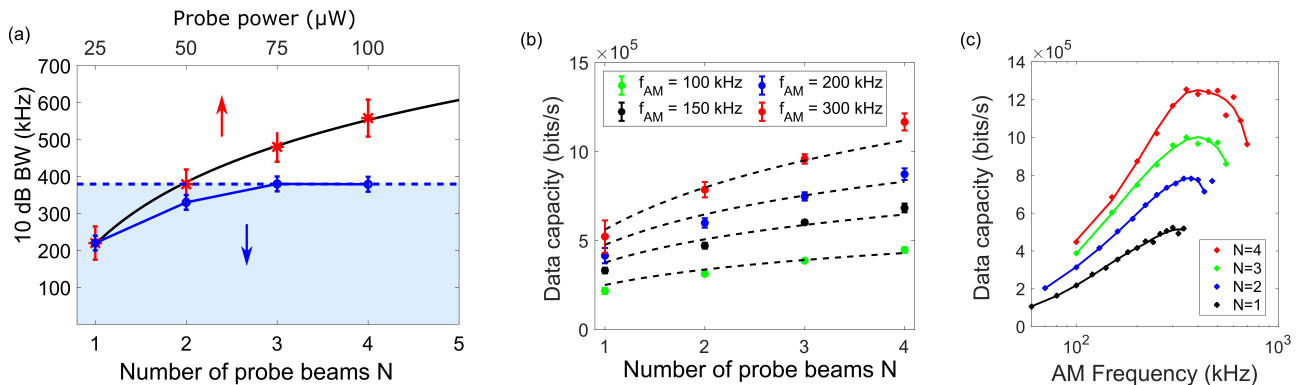


Figure 5. (a) 10 dB bandwidth limit of a single probe beam as function of the probe power (blue, bottom axis) and for multiple beams (red, top axis), where the probe power is distributed equally among N beams. The BW increases with logarithmically (black line), and surpasses the BW limit of the single beam (shaded area). (b) Data capacity for four different AM frequencies and up to four probe beams. The dashed lines show the theoretical scaling of Eq. (3), where $\text{SNR}_{N=1}$ was calculated from the experimental data for $N = 3$. (c) Data capacity versus amplitude modulation frequency for N beams.

AOM. Therefore, we show average values of all four probe beam combinations in Figs. 4 and 5. Deviations between the detected SNR_{dB} for different probe frequencies are caused by a change in the EIT condition. The main contribution comes from slightly different beam waists in the overlap area, affecting the ratio Ω_c/Ω_p . To illustrate the change of the EIT transmission for different probe frequencies, we present in Fig. 6 the EIT profiles for a scan of the coupling beam frequency. The AOM-offset of the probe frequency with respect to the two-level resonance frequency is denoted as Δ . For all frequencies we observe two EIT peaks, since the EIT condition can be met for the $52D_{5/2}$ and $52D_{3/2}$ Rydberg states. Relevant in this investigation is the larger peak. For a fixed probe power of $300 \mu\text{W}$ the height of the EIT peak changes with Δ , since the position of the probe beam in the focal plane moves as $\sim \Delta \times 37 \mu\text{m}/\text{MHz}$. Considering the angle be-

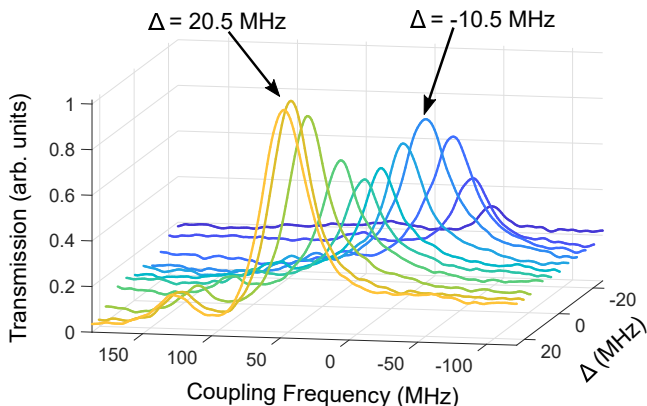


Figure 6. Probe transmission for different AOM driving frequencies Δ (EIT resonance at $\Delta = 0$) at a fixed probe power of $300 \mu\text{W}$. The coupling laser frequency is scanned and the frequency axis calibrated using the known splittings between the states $52D_{5/2}$ (large peaks) and $52D_{3/2}$ (smaller peaks on the left side).

tween the counter-propagating probe and coupling beam, and a scan of $\Delta = 40$ MHz the overlap areas are separated by up to 40 mm, which is approximately twice as large as the Rayleigh lengths of the probe and coupling beam. The appearance of two maxima at $\Delta = -10.5$ MHz and $\Delta = 20.5$ MHz suggests that the focal plane of probe and coupling beam do not coincide. For the probe frequencies f_1 to f_4 of Fig. 4(b) the EIT peak height differs by 10% for a fixed probe power, which translates to deviations in the SNR_{dB} . This technical limitation can be mitigated, for example by adjusting the probe power of individual beams.

3. SNR_{dB} for different probe beam frequencies

With the objective to find optimised probe frequencies for our system, the coupling laser was locked to the $5P_{3/2} \leftrightarrow 52D_{5/2}$ transition and the probe frequency swept over a 40 MHz range using the AOM. In difference to the measurements in Fig. 6, we allow for changes in the probe power with AOM driving frequency, which is caused by the dependence of the AOM efficiency on the driving frequency. The SNR_{dB} was determined as a function of the AOM frequency (probe frequency) for an amplitude modulated MW field at 100 kHz. The results are presented in Fig. 7(a)-(c) as blue data points. In our frequency scan, we observe two minima ($\Delta = -12$ MHz and $\Delta = 5$ MHz), which can be associated with points for which the EIT transmission does not change in presence of the MW field. High SNR_{dB} occurs for the largest change in probe transmission due to the applied MW field. For a symmetric AT profile, as depicted in Fig. 7(d), we expect a symmetric scenario in Fig. 7(a)-(c) with three peaks with a vertical line symmetry at the resonance frequency $\Delta = 0$, and e.g. observed in¹⁵. A number of factors can lead to the observed asymmetry in Fig. 7(a)-(c). First, with our MW electric field we intend

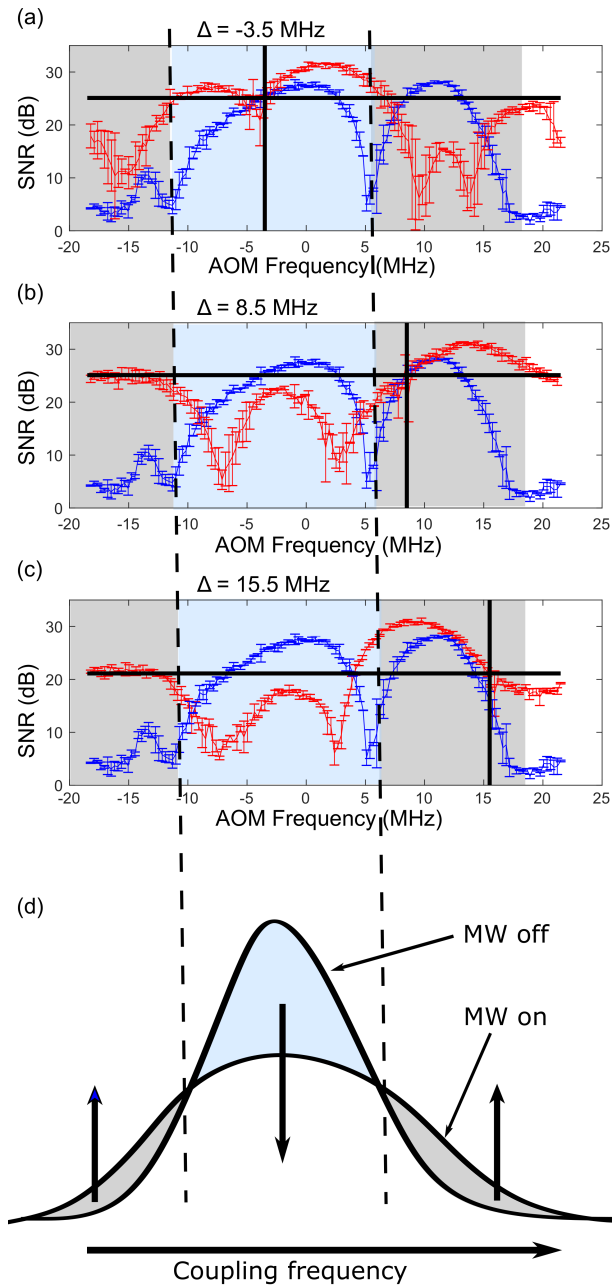


Figure 7. SNR_{dB} as function of the AOM frequency for a single beam (blue) and an additional beam (red) with frequency detuning (a) -3.5 MHz, (b) 8.5 MHz, and (c) 15.5 MHz - represented by the vertical black lines. The SNR_{dB} of the beam at frequencies (a)-(c) is represented as horizontal black line. A schematic representation of the EIT spectrum with and without MW field for a scan of the coupling laser frequency is shown in (d).

to couple the Rydberg states $52D_{5/2} \leftrightarrow 51F_{7/2}$ which has transition dipole moments up to $2260 a_0 e$. However, a second Rydberg state, $51F_{5/2}$, is located only 1.2 MHz away and can shift the AT-profile. Secondly, the probe frequency is scanned using an AOM with maximised diffraction efficiency at the resonance $\Delta = 0$. Lastly,

the EIT peak height decreases rapidly for frequencies $\Delta < -10$ MHz, as shown in Fig. 6, due to weaker overlap of coupling and probe beam. This explains the difference in height of the left and right peak in Fig. 7(a)-(c).

4. Effect of an additional probe beam

In order to characterise the performance with multiple probe beams, we scanned the frequency of the first probe beam in presence of a second probe beam at three fixed frequency detunings -3.5 MHz, 8.5 MHz and 15.5 MHz. We measured the SNR_{dB} of the two beams by combining the two probe signals on the photodetector. The obtained values of SNR_{dB} are presented in red in Fig. 7(a)-(c). One could naively expect the SNR_{dB} to remain at least at the value given by the fixed-frequency beam, depicted in Fig. 7(a)-(c) as horizontal black lines. Instead, for two probe beams we predominantly observe a drop in the SNR_{dB} if the two probe frequencies are in differently shaded frequency areas (grey and blue), and a rise for two frequencies in identically shaded areas. A descriptive explanation for this phenomenon is given in Fig. 7(d). While the grey and blue areas both show a significant change of the EIT signal in presence of a MW electric field, for grey areas the probe transmission increases in height, whereas the signal drops in the blue area. By detecting both beams on the same photodetector the transmission signals from two beams can be effectively “out of phase”. If both components are equally strong, a zero occurs in the SNR_{dB} . Otherwise, the stronger signal dominates the scenario. Hence, for our experimental setup it is crucial to choose frequencies within identically colored areas. All beams can then be detected with a simple detection scheme, involving only a single photodetector. Alternatively, the probe transmission signal can be detected with individual photodetectors to allow for less sensitivity in the choice of probe frequencies. For the SNR_{dB} measurements of up to four distributed beams, we used a separation of $3 - 4$ MHz for adjacent probe beams centered around $\Delta = 0$. With this choice the individual beams have similar SNR_{dB} levels, as well as spatially separated overlap areas.

We note that the frequency deviations of the probe beams in our setup could be of potential benefit for a MIMO configuration. For the generation of multiple probe beams with identical frequencies electromechanically driven mirrors or liquid crystal deflectors could be implemented.

IV. DISCUSSION

The fastest switching time in an atom-based receiver is given by the contrast of optical transmission and the detection noise. Using purely classical light sources, the noise floor is ultimately limited by the photon shot noise, while the transmission contrast is determined by the life-

time of a single atom in a dark state, the number of contributing atoms in the EIT process, and the input probe beam power. The atom-switching time in our realisation is primarily limited by the available coupling laser power. This can be expressed in terms of the EIT pumping rate $\Omega_{\text{EIT}} = \Omega_c^2/2\Gamma^7$, which describes the time atoms need to re-establish the EIT dark state when the MW field is turned off.

For a given realisation with a particular atom-switching time, one expects that increasing the probe power or the number of the participating atoms within the receiver volume would lead to a larger contrast in optical transmission, and therefore increase the SNR. We observe that the SNR reaches a maximum beyond a certain probe power and for a given atomic volume, but by spatially distributing the probe power to address different atoms, one can increase the SNR, which ultimately leads to an increase of the data capacity. Our results demonstrate a scaling of the data capacity with $C_{\text{SIMO}} = \text{BW} \times \log_2(1 + N \times \text{SNR})$ for N probe beams. For a single receiver with a probe power that equals the sum of the distributed probe beams power broadening of the intermediate state occurs. Furthermore, a higher fraction of atoms are excited to the Rydberg state, which potentially results in additional Rydberg dephasing. These effects are avoided by distributing the probe power among several receivers. Fundamentally, the capacity advantage of the distributed receiver stems from a larger sensing volume, i.e a larger number of atoms contributing to the signal. While we exceed the BW of our single receiver and our data follows the predicted scaling of a SIMO system, the overall achieved data capacity remains low. This originates from low SNR levels of the individual receiver volumes, caused by the angled geometry of our setup, as discussed in Sec. III C 1.

Our results particularly highlight the challenge of scaling up the data capacity of Rydberg atomic receivers by classical means, such as scaling up the receiver volume. To put this in perspective, in order to increase the data capacity by an order of magnitude, one needs to implement more than thirty distributed receivers with the receiver volume larger by the same ratio. Assuming a probe volume of a single receiver to be $\sim 0.3 \text{ mm}^3$, this would require a distributed receiver with a volume of $\sim 1 \text{ cm}^3$. This shows the importance of maximising single-channel data capacity by reducing the detection noise floor, Doppler broadening or by employing collective effects in atomic excitation/de-excitation^{26,27}. Such collective effects have so far remained elusive in warm atomic vapour, but have been demonstrated in cold atomic gases²⁸.

V. CONCLUSION AND OUTLOOK

We have considered a simple setup employing spatially distributed atomic receivers which allows to surpass the SNR limit of an individual atom-based receiver, result-

ing in an improved channel capacity. The concept of receiver arrays has proven beneficial in wireless communication systems for high-speed transmission and increased capacity. For example for a SIMO system, as presented in this work, an increase in channel capacity to $C_{\text{SIMO}} = \text{BW} \times \log_2(1 + N \times \text{SNR})$ ²⁹ for N receiving antennas has been derived. We experimentally confirmed the same scaling for the channel capacity of our atomic-receiver system with N probe beams (receiver volumes). Moreover, we observed a significant increase in SNR_{dB} , and BW – the latter scaling logarithmically for our Rydberg atom-based RF-to-optical receiver. We showed that such enhancement of the BW cannot be obtained by a single receiver with an identical beam geometry and a similar level of combined optical power due to the saturation of the EIT peak transmission. Our approach benefits from the little additional resource overhead needed to add multiple probe beams, if generated by the first order of an AOM and a multitone frequency source. While the results shown in this work were carried out with $N \leq 4$ probe beams, the number of beams can easily be expanded³⁰.

In the future we plan to extend the system with additional transmitter RF antennas in a configuration where the receivers can distinguish between transmitters. This will allow us to realise a multi-input-multi-output (MIMO) system, promising further enhancement in channel capacity. For an additional transmitter antenna, we expect an improvement in channel capacity with $2 \times \log_2(1 + N \times \text{SNR})$. This however requires that the spatial separation between the distributed atomic receivers to be in the order of the RF wavelength¹⁹. Furthermore, we might be able to boost the coupling beam power for our setup e.g. using power buildup in a resonant cavity.

ACKNOWLEDGMENTS

We acknowledge funding from the Marsden Fund of New Zealand (Contract No. UOO1729) and MBIE (Contract No. UOOX1915).

DATA AVAILABILITY

The data that support the findings of this study are available from the corresponding author upon reasonable request.

Appendix A: Noise assessment of the AOM

The key component for the generation of multiple probe beams in our experimental setup is a continuously running AOM, see Fig. 2(a). This AOM is the main source for noise, degrading our SNR_{dB} measurements. In general, two sources of noise can be induced by an

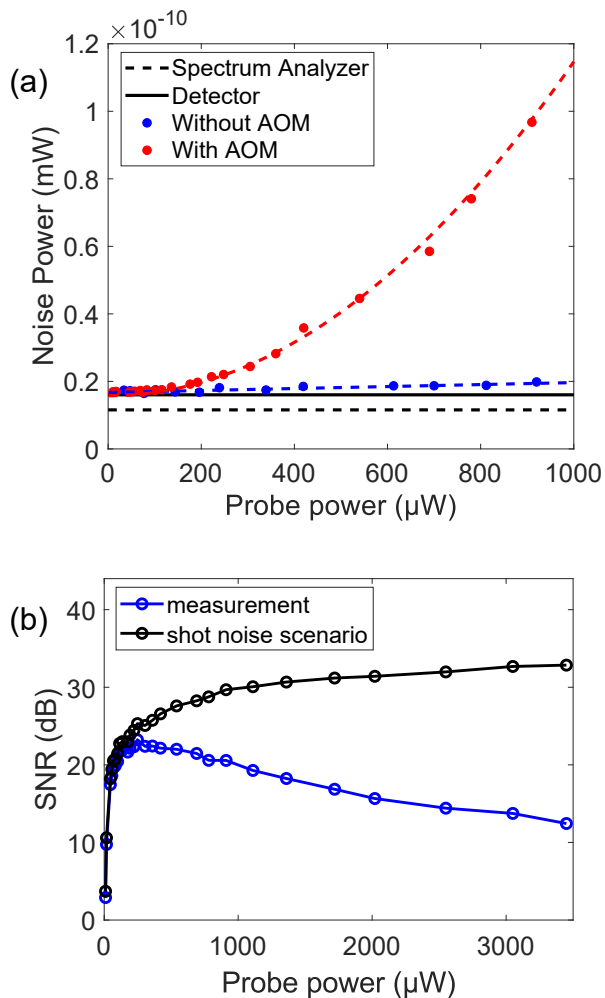


Figure 8. (a) Measurement of the noise power on the spectrum analyser over a frequency band of 50 to 350 kHz for a resolution bandwidth of 3 kHz and different probe powers. The data points show average values over the frequency range for the first order of the AOM (red) and for a measurement without AOM (blue). The noise floor of the photodetector (black line) lies ~ 1.5 dB above the noise floor of the spectrum analyser (dashed line). (b) Development of SNR_{dB} as function of probe power as shown for our setup in Fig. 3. If only shot noise is present (black), the SNR_{dB} reaches a maximum of ~ 32 dB.

AOM: phase noise from the AOM driver and RF amplifier, and intensity noise. The intensity noise, which originates from relative diffraction efficiency fluctuations (RDEF)³¹, dominates in our setup. A measurement of the noise power on the spectrum analyser over a range of 50 to 250 kHz with a resolution bandwidth of 3 kHz and for different probe beam powers is shown in Fig. 8(a). The red data points represent a measurement in which the first order of the AOM ($\sim 65\%$ efficiency) was detected on the photodetector (Thorlabs PDA 100A-EC, bandwidth up to 2.4 MHz) and the optical power incident on the AOM was varied. We find that the noise power scales as quadratic function of the probe power. In a

consecutive measurement (blue) the AOM was removed from the beam path, resulting in a linear increase of noise power with increasing probe power. A shot noise limited scenario (3 dB gain above the detector noise floor) is reached for probe powers > 4 mW.

The intensity noise of the AOM limits the achievable SNR_{dB} as depicted in Fig. 8(b) (blue points). Towards higher probe powers the peak height of the AM signal, see Fig. 3(a), reaches its maximum while the noise floor increases quadratically with the probe power, resulting in a fall-off of the SNR_{dB} . If we compensate for the increasing noise floor and only consider shot noise (black points) the SNR_{dB} reaches a maximum of ~ 32 dB, and overall a higher SNR_{dB} can be obtained. In order to reduce the intensity noise of the AOM the RF driving power of the AOM can be set close to its saturation point. To further reduce the noise, alternative options to generate multiple beams can be employed, as discussed in Sec. III C 4. For a photon-shot-noise-limited measurement an optical heterodyne detection scheme can be employed, where a local oscillator beam is mixed with the transmitted probe as e.g. used in²¹.

Appendix B: BW and data capacity for multiple receivers

For a SIMO configuration with N identical receiver volumes (i.e. N probe beams) the signal-to-noise ratio in decibel is given by

$$\text{SNR}_{\text{dB}}(N) = \text{SNR}_{\text{dB},N=1} + 20 \times \log_{10}(N). \quad (\text{B1})$$

This implies that every time the number of receiver volumes, N , is doubled, the SNR in terms of an optical power ratio increases by a factor of two, as can be seen in Fig. 9 for five sets of measurements. These measurements have in common that the SNR of the individual receivers were roughly identical, while the probe power of the beams could vary significantly from receiver to receiver.

The scaling in $\text{SNR}_{\text{dB}}(N)$ relates to an improvement of bandwidth with N as

$$\text{BW}(N) = \text{BW}_{N=1} + 20/m \times \log_{10}(N), \quad (\text{B2})$$

where m is the slope defined by the falloff of the SNR-curves towards higher AM frequencies in Figs. 4(a)-(b). The slope, m , depends on atomic parameters, such as coherence rates and vary for different experimental setups.

The achievable communication rate for a channel at a given amplitude modulation frequency f_{AM} is given by the Shannon-Hartley theorem, Eq. (1), as $C = f_{\text{AM}} \times \log_2(1 + \text{SNR})$. Equation (B1) can be used to derive the theoretical data capacity for N receiver volumes

$$\begin{aligned} C_A(N) &= f_{\text{AM}} \times \log_2[1 + \text{SNR}(N)] \\ &= f_{\text{AM}} \times \log_2[1 + 10^{\text{SNR}_{\text{dB}}(N)/20}] \\ &\stackrel{\text{B1}}{=} f_{\text{AM}} \times \log_2[1 + N \times \text{SNR}_{N=1}], \end{aligned} \quad (\text{B3})$$

where $\text{SNR}_{N=1}$ is the SNR of a single beam as ratio of optical power.

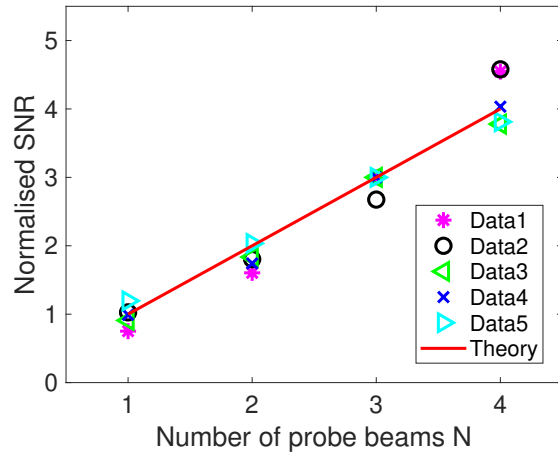


Figure 9. Scaling of the SNR in means of a optical power ratio with the number of probe beams (receiver volumes). The data is normalised to the SNR of a single probe beam.

REFERENCES

- ¹J. Sedlacek, A. Schwettmann, H. Kübler, R. Löw, T. Pfau, and J. Shaffer, “Microwave electrometry with Rydberg atoms in a vapour cell using bright atomic resonances,” *Nature Physics* **8**, 819–824 (2012).
- ²H. Fan, S. Kumar (Gangwar), J. Sedlacek, H. Kübler, S. Karimkashi, and J. Shaffer, “Atom based RF electric field sensing,” *Journal of Physics B: Atomic* **48** (2015), 10.1088/0953-4075/48/20/202001.
- ³C. Holloway, M. Simons, J. Gordon, A. Dienstfrey, D. Anderson, and G. Raithel, “Electric field metrology for SI traceability: Systematic measurement uncertainties in electromagnetically induced transparency in atomic vapor,” *Journal of Applied Physics* **121**, 233106 (2017).
- ⁴M. Jing, Y. Hu, J. Ma, H. Zhang, L. Zhang, L. Xiao, and S. Jia, “Atomic superheterodyne receiver based on microwave-dressed Rydberg spectroscopy,” *Nature Physics*, 1–5 (2020).
- ⁵T. F. Gallagher, “Rydberg atoms,” *Reports on Progress in Physics* **51**, 143–188 (1988).
- ⁶A. B. Deb and N. Kjærgaard, “Radio-over-fiber using an optical antenna based on Rydberg states of atoms,” *Applied Physics Letters* **112**, 211106 (2018).
- ⁷D. H. Meyer, K. C. Cox, F. K. Fatemi, and P. D. Kunz, “Digital communication with Rydberg atoms and amplitude-modulated microwave fields,” *Applied Physics Letters* **112**, 211108 (2018).
- ⁸Z. Song, W. Zhang, X. Liu, H. Zou, J. Zhang, Z. Jiang, and J. Qu, “Quantum-based amplitude modulation radio receiver using Rydberg atoms,” in *2018 IEEE Globecom Workshops (GC Wkshps)* (2018) pp. 1–6.
- ⁹Z. Song, H. Liu, X. Liu, W. Zhang, H. Zou, J. Zhang, and J. Qu, “Rydberg-atom-based digital communication using a continuously tunable radio-frequency carrier,” *Opt. Express* **27**, 8848–8857 (2019).
- ¹⁰C. L. Holloway, M. T. Simons, A. H. Haddab, C. J. Williams, and M. W. Holloway, “A “real-time” guitar recording using Rydberg atoms and electromagnetically induced transparency: Quantum physics meets music,” *AIP Advances* **9**, 065110 (2019).
- ¹¹C. L. Holloway, M. Simons, A. H. Haddab, J. A. Gordon, D. A. Anderson, G. Raithel, and S. Voran, “A multiple-band Rydberg atom-based receiver: AM/FM stereo reception,” *IEEE Antennas and Propagation Magazine* (2020), 10.1109/map.2020.2976914.
- ¹²D. A. Anderson, R. E. Sapiro, and G. Raithel, “An atomic receiver for AM and FM radio communication,” *IEEE Transactions on Antennas and Propagation* (2020), 10.1109/TAP.2020.2987112.
- ¹³M. T. Simons, A. H. Haddab, J. A. Gordon, and C. L. Holloway, “A Rydberg atom-based mixer: Measuring the phase of a radio frequency wave,” *Applied Physics Letters* **114**, 114101 (2019).
- ¹⁴C. L. Holloway, M. T. Simons, J. A. Gordon, and D. Novotny, “Detecting and receiving phase-modulated signals with a rydberg atom-based receiver,” *IEEE Antennas and Wireless Propagation Letters* **18**, 1853–1857 (2019).
- ¹⁵H. Zou, Z. Song, H. Mu, Z. Feng, J. Qu, and Q. Wang, “Atomic receiver by utilizing multiple radio-frequency coupling at Rydberg states of rubidium,” *Applied Sciences* **10**, 1346 (2020).
- ¹⁶D. Petrosyan, J. Otterbach, and M. Fleischhauer, “Electromagnetically induced transparency with Rydberg atoms,” *Phys. Rev. Lett.* **107**, 213601 (2011).
- ¹⁷S. H. Autler and C. H. Townes, “Stark effect in rapidly varying fields,” *Phys. Rev.* **100**, 703–722 (1955).
- ¹⁸C. E. Shannon, “Communication in the presence of noise,” *Proceedings of the IRE* **37**, 10–21 (1949).
- ¹⁹J. R. Barry, E. A. Lee, and D. G. Messerschmitt, *Digital Communication*, 3rd ed. (Springer US, 2004).
- ²⁰Gunasekaran, “Evaluation of multiple input multiple output (MIMO) system capacity with spatial correlations,” *Journal of Computer Science* **7**, 1490–1496 (2011).
- ²¹K. C. Cox, D. H. Meyer, F. K. Fatemi, and P. D. Kunz, “Quantum-limited atomic receiver in the electrically small regime,” *Phys. Rev. Lett.* **121**, 110502 (2018).
- ²²B.-H. Wu, Y.-W. Chuang, Y.-H. Chen, J.-C. Yu, M.-S. Chang, and I. A. Yu, “Enhanced spectral profile in the study of Doppler-broadened Rydberg ensembles,” *Scientific Reports* **7** (2017), 10.1038/s41598-017-09953-0.
- ²³L. Hao, Y. Jiao, Y. Xue, X. Han, S. Bai, J. Zhao, and G. Raithel, “Transition from electromagnetically induced transparency to Autler–Townes splitting in cold cesium atoms,” *New Journal of Physics* **20**, 073024 (2018).
- ²⁴P. R. S. Carvalho, L. E. E. de Araujo, and J. W. R. Tabosa, “Angular dependence of an electromagnetically induced transparency resonance in a doppler-broadened atomic vapor,” *Physical Review A* **70**, 063818 (2004).
- ²⁵In configurations with $\theta = 0^\circ$ the overlap area of the probe and coupling beam in the vapour cell is larger. However, as the coupling and probe beam are usually focused to a small spot size, the volume contributing the most to the EIT signal is comparatively small, due to the shorter Rayleigh lengths.
- ²⁶R. H. Dicke, “Coherence in spontaneous radiation processes,” *Phys. Rev.* **93**, 99–110 (1954).
- ²⁷C. Kwong, T. Yang, M. Pramod, K. Pandey, D. Delande, R. Pierrot, and D. Wilkowski, “Cooperative emission of a coherent superflash of light,” *Physical Review Letters* **113**, 223601 (2014).
- ²⁸C. Möhl, N. L. R. Spong, Y. Jiao, C. So, T. Ilieva, M. Weidemüller, and C. S. Adams, “Photon correlation transients in a weakly blockaded Rydberg ensemble,” *Journal of Physics B: Atomic, Molecular and Optical Physics* **53**, 084005 (2020).
- ²⁹E. Ghayoula, A. Bouallegue, R. Ghayoula, and J.-Y. Chouinard, “Capacity and performance of MIMO systems for wireless communications,” *Journal of Engineering Science and Technology* **7**, 108–111 (2014).
- ³⁰K. O. Roberts, T. McKellar, J. Fekete, A. Rakonjac, A. B. Deb, and N. Kjærgaard, “Steerable optical tweezers for ultracold atom studies,” *Opt. Lett.* **39**, 2012–2015 (2014).
- ³¹F. Liu, L. Gu, S. Xie, X. He, D. Yi, M. Zhang, and Q. Tao, “Acousto-optic modulation induced noises on heterodyne-interrogated interferometric fiber-optic sensors,” *Journal of Lightwave Technology* **36**, 3465–3471 (2018).